NANO · MICRO small
www.small-journal.com

Defects in Hard Carbon: Where Are They Located and How Does the Location Affect Alkaline Metal Storage?

Emilia Olsson, Jonathon Cottom, and Qiong Cai**

Hard carbon anodes have shown significant promise for next-generation battery technologies. These nanoporous carbon materials are highly complex and vary in structure depending on synthesis method, precursors, and pyrolysis temperature. Structurally, hard carbons are shown to consist of disordered planar and curved motifs, which have a dramatic impact on anode performance. Here, the impact of position on defect formation energy is explored through density functional theory simulations, employing a mixed planar bulk and curved surface model. At defect sites close to the surface, a dramatic decrease (≥50%) in defect formation energy is observed for all defects except the nitrogen substitutional defect. These results confirm the experimentally observed enhanced defect concentration at surfaces. Previous studies have shown that defects have a marked impact on metal storage. This work explores the interplay between position and defect type for lithium, sodium, and potassium adsorption. Regardless of defect location, it is found that the energetic contributions to the metal adsorption energies are principally dictated by the defect type and carbon interlayer distance.

1. Introduction

The increase in global energy demand has necessitated the development of efficient and sustainable energy storage technologies. Rechargeable batteries play a crucial role in providing energy storage needed to transition from a fossil-fuel-based to a sustainable energy economy.[1,2] Alkali ion batteries including lithium (Li)-ion batteries (LIBs), sodium (Na)-ion batteries (NIBs), and potassium (K)-ion batteries (KIBs) have received increasing attention as rechargeable batteries.[1,3,4] Na and K are among the most abundant elements, making them promising and suitable complements to Li whose resources are rapidly declining with increasing energy demands.[5] For the next-generation batteries to emerge, optimization of the anode material needs to be achieved. Hard carbons (HCs) are promising alkali ion metal battery anodes,[6,7] and have been successfully synthesized from biomass, making this anode material interesting from a sustainability and circular economy perspective.[8] Currently, HC anodes are limited by their poor rate capability, irreversible capacity loss, and insufficient voltage.[7,9] To improve the HC anode performance, atomic scale structural understanding is essential.

HCs are complex nanoporous disordered nongraphitizable materials consisting of randomly oriented, curved, and defective graphene nanosheets (sometimes also referred to as fullerenic) with varying interlayer distances.[7,10,11] The structure consists of sp^2-hybridized carbons in a hexagonal pattern, with pentagons, defects, and sp^3-hybridized carbons interspersed throughout the structure.[11–14] A variety of defects have been shown to exist in the graphenic sheets such as carbon vacancies and heteroatom defects.[11,14,15] High-resolution transmission electron spectroscopy images of HC structures show curved regions that are randomly interlinked, with rumpling leading to the formation of a domed surface.[16] These curved regions are interpreted as randomly stacked graphene layers arching as a result of strain or packing, with highly defective and disordered structures.[16–20] Metal ions can store at defects both at basal plane and edge sites, within pores, and in between the turbostratically stacked expanded graphitic layers.[7,21–23] During electrochemical cycling, the increased capacity observed for HC anodes is attributed to surface defects, adsorption at basal plane defects, metal deposition in pores, and bond formation with heteroatoms.[6,10,22] The surface adsorption contributing to metal ion storage and the voltage profile is dependent on the HC surface, which is in contact with the electrolyte.[9,10,23,24] The HC surface can vary greatly between different HCs. These differences are attributed to the synthetic method and the presence of defects and heteroatoms.[9,10,14,23,25,26] Furthermore, cross-linking of the sp^2-hybridized carbon layers through sp^3-hybridized carbon atoms has been observed in HC materials from their Raman spectra.[1,6,24] Deciphering the interplay between these motifs is challenging but vital in developing an understanding of HC as an anode material.

HCs from different precursors have been shown to have markedly different structures and heteroatom contents.[6,7,22,27]

Dr. E. Olsson, Dr. Q. Cai
Department of Chemical and Process Engineering
University of Surrey
Guildford GU2 7XH, UK
E-mail: k.olsson@surrey.ac.uk; q.cai@surrey.ac.uk
Dr. J. Cottom
Department of Physics and Astronomy
University College London
London WC1E 6BT, UK
The ORCID identification number(s) for the author(s) of this article can be found under https://doi.org/10.1002/smll.202007652.

DOI: 10.1002/smll.202007652

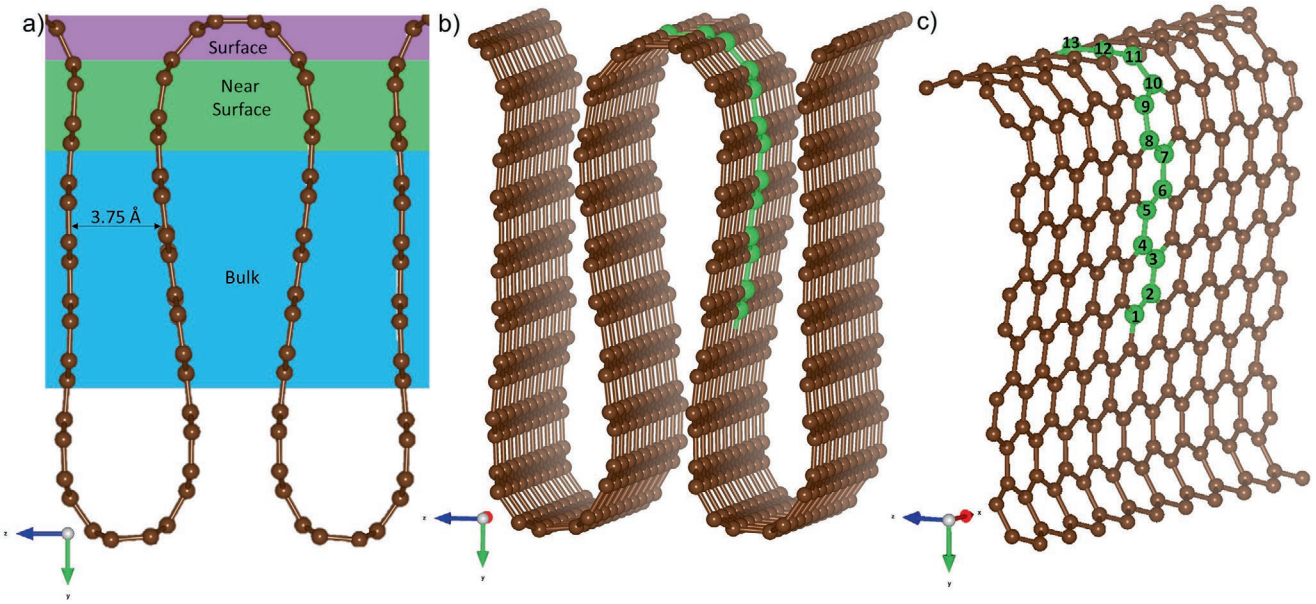

Figure 1. Schematic representation of a) the different regions (bulk-like, near-surface-like, and surface-like) in the simulation cell as defined in this paper, and b) pristine simulation cell with brown spheres being carbon atoms and green spheres signifying the carbon atoms at c) the general defect positions. Red arrows indicate the *x*-direction, green the *y*-direction, and blue the *z*-direction.

Pyrolysis of precursors such as sugars, biomass, or phenolic resins releases heteroatoms, and the heteroatom concentration decreases with thermal treatment temperature.[6,7,10,23] Even HCs with similar structure but with different defect concentrations show markedly different NIB cycling behaviors, making the consideration of defects imperative.[23] Furthermore, heteroatom doping, annealing, and defect engineering as a means to improve the anode performance have been reported.[9,15,28,29] However, contrasting reports on the effect of these defects on anode performance exist and further atomic-scale study is required to understand the role of individual defects.[9,30,31] The complex and varying structure of HC makes the modeling of a universal HC material unfeasible.[9] Breaking the HC material down into simpler structural motifs allows the individual structural features found in many HCs to be understood in isolation. Previously, we have studied defects on the basal plane (using graphene as a model for this structural motif), cylindrical pores (using carbon nanotubes as a model for curved motifs), and planar graphitic pores (using bilayer graphite as a model for the graphitic stacks with varying interlayer distances).[7,21,32–35] In this paper, we consider more complex HC models, to include the effect of edges, curvature, and strain on the defect formation. These models are based on the reconstructed graphite (10–11) surface, which we have employed previously to study metal binding at the transition from curved to planar carbon morphologies. The interlayer distances in the planar region (corresponding to stacked graphitic layers) have been chosen to reproduce the experimental mean separation and range.[7,21,33,36] This approach allows for the motifs found in HC materials to be modeled in a systematic way. Furthermore, these models are relevant for other carbon materials based on graphite, carbon nanotubes, and graphene as these all share common structural features. This handling allows us to study the defect formation as a function of lattice position and the effect of defect position on the initial alkali metal (Li/Na/K) incorporation.

2. Results and Discussion

From experimental evidence, carbon-based anodes have both curved and planar motifs, with surfaces and their defects having a particular influence on electrolyte breakdown and the initial metal adsorption.[7,11,36–39] These curved pores have been observed both from pair distribution analysis and transmission electron microscopy imaging.[7,11,36–38] In this study, we investigate the effect of these morphologies on defect formation as a function of lattice position. Based on our previous investigation of defect formation on graphene,[32,34] the following defects are considered: carbon vacancy (V_C), nitrogen substitutional or graphitic nitrogen defect (N_C), nitrogen substitutional defect and carbon vacancy or pyridinic nitrogen defect (N_CV_C), oxygen substitutional defect (O_C), double oxygen substitutional defect ($2O_C$), oxygen substitutional defect and carbon vacancy (O_CV_C), triple oxygen substitutional defect ($3O_C$), nitrogen and oxygen substitutional defect (N_CO_C), and double oxygen single nitrogen substitutional defect (N_C2O_C).[7,32,34] The curved carbon models used in this work are based on the reconstructed graphite models previously developed by Lechner et al. and Thinius et al.[20,40] The pristine model consists of 800 carbon atoms, with an average interlayer separation of 3.75 Å (ranging from 4.04 Å at defect position 1 to 3.09 Å at defect position 8) based on previous small angle X-ray scattering/wide angle X-ray scattering characterization of HC anode materials.[7,21,33,36] The defects highlighted above are then considered in this system at various distances from the carbon surface, which will henceforth be referred to as position *X* (shown in **Figure 1**). This allows for consideration of defect formation in graphitic stacks (highlighted in Figure 1a as the bulk), in the transition region between intercalation and surface behavior (highlighted in Figure 1a as the near surface), and finally at the curved surface.

The defect formation energy (E_f^{defect}) can be used as a measurement of defect concentration (the lower the E_f^{defect} the higher

the equilibrium concentration) at equilibrium conditions, and gives an indication of the probability distribution of defects.[41–45] Following the well-established methodology of Zhang and Northrup, E_f^{defect} can be calculated from Equation (1)[41]

$$E_f^{defect} = E_{defective} + \sum n_i \mu_i - E_{bulk} \quad (1)$$

$E_{defective}$ is the total energy of the defective carbon model, E_{bulk} is the total energy of the nondefective carbon model, n_i is the number of defect species either added or removed in relation to the pristine model, and μ_i is the chemical potential of N, O, and C, respectively. Assuming equilibrium conditions (which is not necessarily the case during the synthesis of these materials), E_f^{defect} can be used to form an understanding of the relative probability distribution and concentration of these defects at different temperatures. These are plotted in Figure S1 (Supporting Information) as a function of position for a single defect, and as an ensemble of all defects in Figures S2–S5 (Supporting Information).[41–45]

Carbon vacancies, and oxygen and nitrogen heteroatom defects, respectively, are commonly found in carbon-based materials and have been identified from X-ray photoelectron spectroscopy (XPS), Raman, and in situ experiments of graphene,[14,46–48] and XPS and Raman measurements of HCs.[7,8,36,49,50] Although the presence of these defects in HC anode materials has been confirmed, their exact form and location, and their subsequent effect on lithiation, sodiation, and potassiation require atomic-scale handling. It is important to note here that both nitrogen and oxygen can be introduced to these materials as performance enhancing dopants, and hence defects in this context does not necessarily give negative effects, but could be sought from a material engineering and optimization point of view. In the next sections, we investigate how these different defects change as a function of lattice position in terms of structure and defect formation energy. This will allow for an understanding of carbon, oxygen, and nitrogen defect concentrations under equilibrium conditions at both curved surfaces and in graphitic stacks.

2.1. Carbon Vacancy (V_C)

The calculated E_f^{defect} are shown in **Figure 2**a where the blue oval highlights V_C in the bulk-like position with little (or no deviation) from the bulk defect with the E_f^{defect} remaining in a tight (<0.2 eV) range. As the surface is approached, E_f^{defect} decreases dramatically (≈50% decrease), with a 3.81 eV reduction in E_f^{defect} with respect to the bulk E_f^{defect}. The dramatic decrease in surface E_f^{defect} results predominately from the disruption of the π-system because of the curvature inherent at the surface (Figure 2b). There is a further reduction in E_f^{defect} as a result of a small expansion in the C—C bonds as the surface is approached (+1–2%), reducing the steric repulsion (Figure 2c,d and Table S1 (Supporting Information)). Hence, on an energetic basis, it would be reasonable to expect dramatically more surface or near surface V_C defects than bulk V_C defects (Figure 2a and Figures S1a and S2 (Supporting Information)).

From a structural perspective, removal of a C-atom from the lattice results in three equivalent C-dangling bonds, which after relaxation form a 5-membered ring and a single C-dangling bond (Figure 2c and Figures S6 and S7 (Supporting Information)). The C—C separation of the 5-membered ring is 2.0 Å (Figure 2c label 1, and Figure 2d), while the C—C separation of the dangling bond is 2.6 Å (Figure 2c labels 2 and 3, and Figure 2d). The most significant geometric change between the bulk and surface V_C defect is the reduction in the C—C bond length (≈25% contraction) in the 5-membered rings (Figure 2d). This is matched by an increase (≈33%) in C—C separation of the dangling bond (Figure 2d and Figure S7 and Table S1 (Supporting Information)). A full list of the C—C bond lengths and separations is included in Figure S7 and Table S1 (Supporting Information). In the bulk position, the V_C defect has three degenerate Jahn–Teller distortions (which has previously been observed for carbon monovacancies in graphene[51–54]), and the 5-membered ring is equally likely to form between any of the C-dangling bonds. The introduction of the curved surface breaks the threefold symmetry of the system and gives rise to two degenerate configurations and one distinct configuration. In defect positions 1–4, there is no energetic difference between these configurations. As the V_C defect is moved toward the surface, the differences between configurations becomes significant at positions 8–13 (Figure 2d and Figure S7 and Table S1 (Supporting Information)). It should be noted that after position 8, the initial positional degeneracy breaks further upon relaxation. V_C at position 8 is further worthy of more consideration as it is the only configuration that shows cross-linking between adjacent graphene sheets (Figure 2e,f). The degree of cross-linking in HC anodes is from experimental evidence dependent on the initial precursors and the intermediate states in the pyrolysis stages.[1,11] From these density functional theory (DFT) simulations, cross-linking is a surface effect and only observed where the curvature brings the sheet separation to a minimum and the dangling bond is pointing toward the neighboring graphene sheet (Figure 2f). Interlayer distances of <3.7 Å are observed in HC anodes,[7,21] as well as cross-linking between graphitic regions,[1] supporting these computational results. A series of nudged elastic band calculations were performed to identify the transition state and barrier height. These calculations show the process to proceed via a low barrier in the forward direction (C—C forming $E_{a\text{-forward}}$ = 0.2 eV, and C—C breaking $E_{a\text{-reverse}}$ = 0.9 eV), although it is important to note that these barriers are highly sensitive to layer separation. Any processes giving rise to these cross-linked motifs are potentially vital in understanding the breakdown of the electrolyte at surface defects in HCs, and more generally for the stability of a given HC and its associated solid electrolyte interphase.

2.2. Nitrogen Defects

Nitrogen doping of HCs can increase carbon surface wettability to the electrolyte, improving battery performance and metal ion storage capacity.[55,56] Nitrogen defects in carbon materials are commonly found as pyridinic, graphitic, and pyrrolic. Pyridinic is referred to here as the N_CV_C defect, where the nitrogen heteroatom is introduced at a carbon lattice site bonded to two carbon atoms in a 6-membered ring together with an adjacent carbon vacancy. Graphitic is referred to as the N_C defect, where the nitrogen heteroatom is sitting at a carbon lattice site bonded to three carbons. Pyrrolic is not considered in this work, which is the nitrogen heteroatom bonded to two carbon

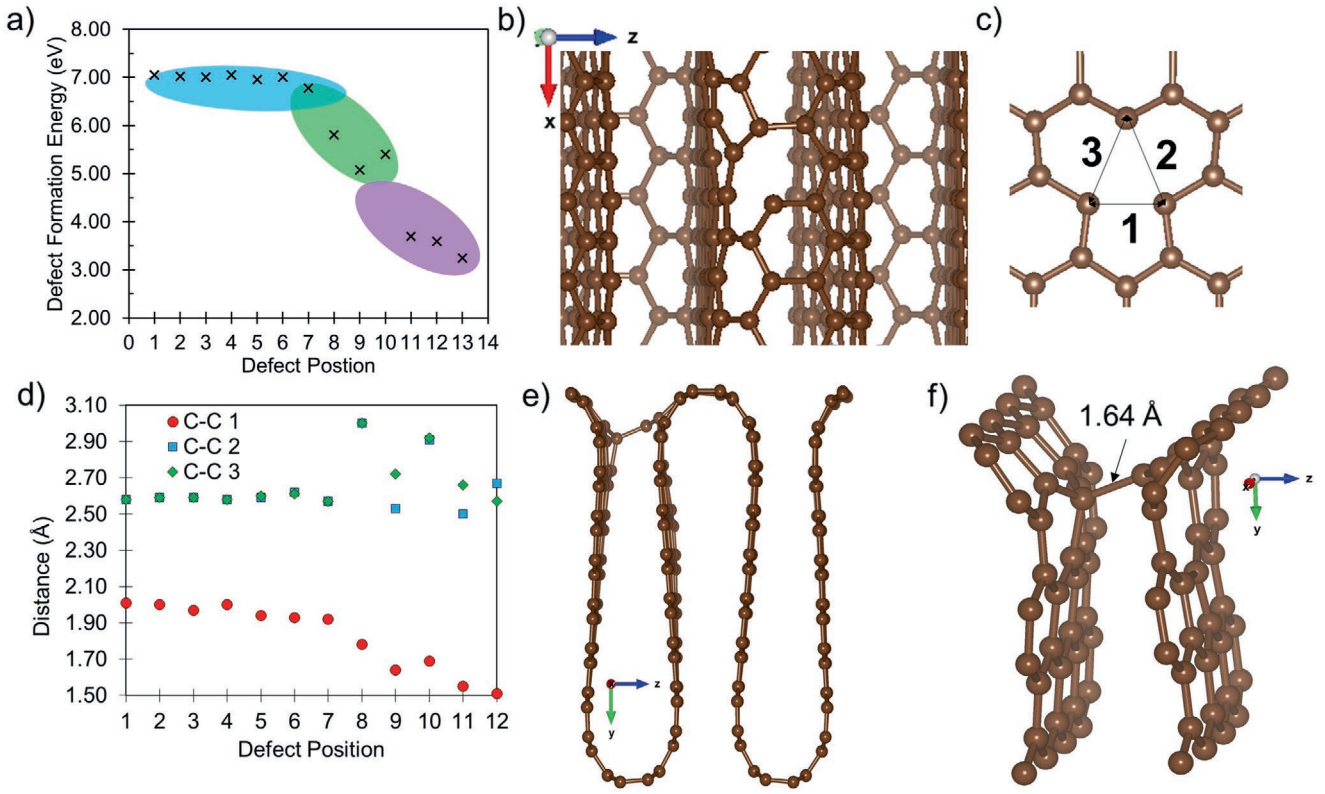

Figure 2. a) Defect formation energies at different lattice positions for the V_C defect. The blue, green, and purple ovals indicate bulk, near surface, and surface positions, as specified in Figure 1. b) Optimized structure of V_C at defect position 11 (all optimized structures are included in Figure S6 in the Supporting Information), c) showing the labeling of the C—C interatomic distances around the defect site, d) the interatomic distances in (c) for the V_C defect at different defect locations, and e) defect position 8 showing the cross-linking. f) A zoomed in view of this structure is provided. Brown spheres are carbon.

atoms in a 5-membered ring, opening up the adjacent 6-membered carbon rings.[57,58] Previous work has demonstrated that the N_C and N_CV_C defects are more energetically stable in graphene and carbon nanotubes (which are similarly curved to the surface sites in the model used here) than the pyrrolic defect,[59] and hence the nitrogen defects considered here are limited to the graphitic and pyridinic nitrogen defects. Substituting one carbon atom for a nitrogen forms the N_C defect (**Figure 3**a,c,d and Figure S8 (Supporting Information)). N_C is incorporated at the carbon lattice site with negligible distortion and has been widely studied as a dopant in sp^2 carbon lattices.[60,61] The N_CV_C defect is geometrically similar to the V_C defect, with the C_6 ring next to the V_C replaced by a C_5N ring (Figure 3b,e–g and Figures S10 and S11 (Supporting Information)). This defect requires additional configurations (as compared to the N_C defect) to be considered (Figure 3e,f and Figure S12 (Supporting Information)), with perpendicular and tilted variants, and the positional a and b type configurations with the N-atom at the top or bottom of the defect, respectively (Figure 3e,f and Figures S9–S12 (Supporting Information)).

E_f^{defect} calculated at different defect positions (Figure 3a) show very similar values for the N_C defect (with a maximum difference of 0.2 eV) regardless of defect location. The N_C defects closer to the surface have a lower E_f^{defect} (0.12–0.2 eV with respect to the bulk N_C) but the differences are an order of magnitude less compared to the other defects considered in this work. The reduction in E_f^{defect} is linked to the site strain, which increases as the curved surface is approached in this model, and by extension how easily the heteroatom can be incorporated at the lattice site. As a result of the negligible surface effect on E_f^{defect}, there is no thermodynamic basis to expect an enhanced concentration of N_C at the surface as compared to the bulk. The highest E_f^{defect} are found in the region directly below the surface, it would be reasonable to expect an, albeit, small reduction in N_C concentration in these regions (Figures S1b and S2, Supporting Information). For the N_C defect, the structural changes with respect to defect position are less pronounced (**Figure 4**a). The N atom sits at the 3-coordinated carbon lattice site with a small contraction of each N—C bond (1.41 Å) with respect to the C—C bond (1.42 Å), although it is important to note that this contraction of bond length is <1% when compared to the pristine carbon lattice (Figure 4a). The presence of the surface has little effect on the defect geometry with the N—C bond showing the same surface bond length expansion as the neighboring C—C, with the same symmetry dependence (Figure 4a and Table S2 (Supporting Information)).

For the N_CV_C defect on the other hand (Figure 3b), there is a clear trend with respect to defect position. As opposed to N_C and V_C, the N_CV_C defect shows several cross trends. These can be understood by separating out the different defect orientations and configurations (Figure 3e,f and Figures S9–S12 (Supporting Information)). In the bulk region (Figure 3b,g blue oval), the E_f^{defect} sit in a narrow 0.4 eV range. The surface/near surface region (highlighted as green and violet in Figure 3b)

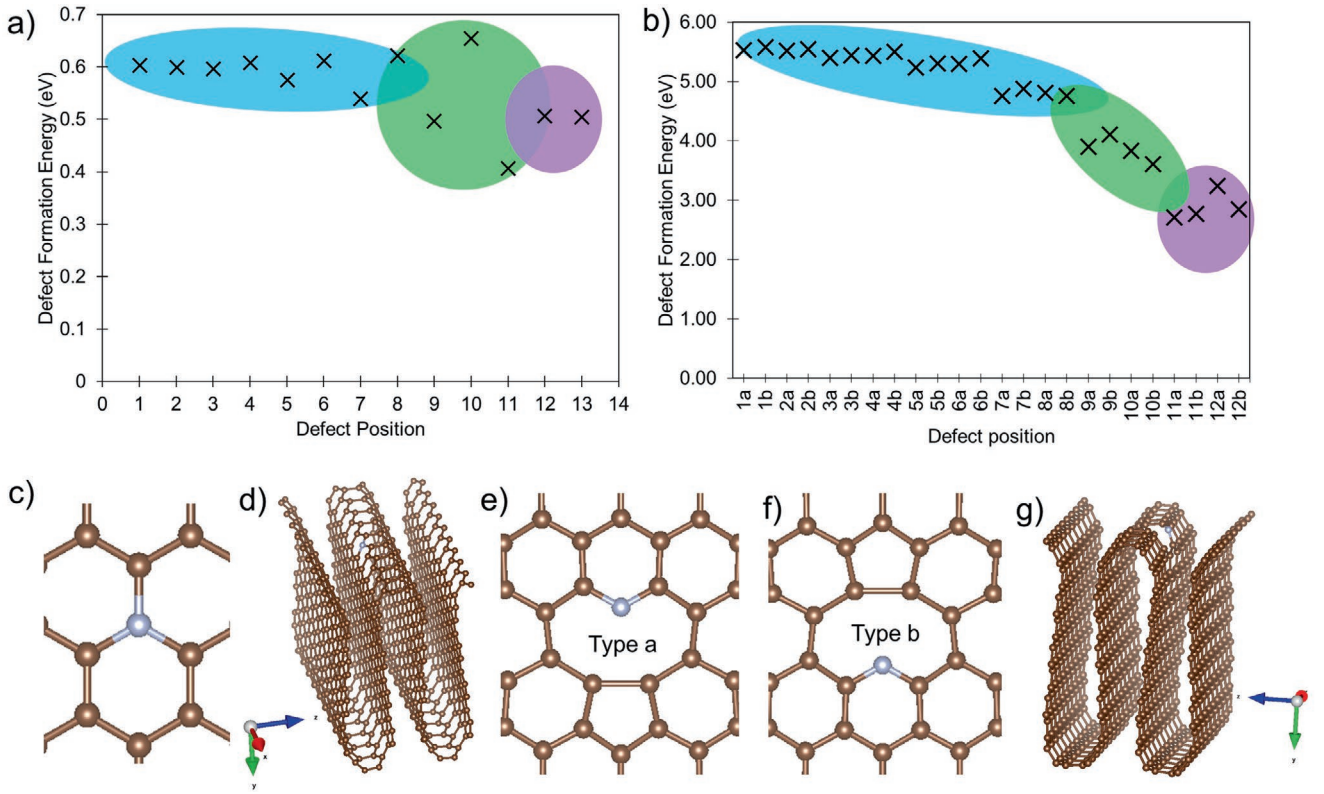

Figure 3. Defect formation energies at different lattice positions for the a) N_C and b) N_CV_C defects. The blue, green, and purple ovals indicate bulk, near surface, and surface positions, as specified in Figure 1. c) The N_C defect structure and d) the same defect at defect position 11. e) The type a and f) type b N_CV_C configurations. g) The optimized structure of N_CV_C at defect position 11a. Carbon atoms are brown spheres, and gray nitrogen.

shows a more marked decrease in E_f^{defect} with a drop of 2.5 eV when compared to the bulk E_f^{defect}. The lowest energy configuration is found at defect positions 11a (Figure 3g) and 11b, which are positioned directly below the surface. The absolute magnitudes of the E_f^{defect} for the N_CV_C defect are still significant, so even the lowest energy configuration has an E_f^{defect} of 2.71 eV, substantially higher than the N_C E_f^{defect} but lower than the V_C E_f^{defect}. However, with a significant reduction (≈50%) in E_f^{defect} as the N_CV_C defect position approaches the surface (as compared to the bulk defect positions), a higher concentration of these defects in the surface and near surface regimes would be anticipated (Figures S1c and S3, Supporting Information).

In the N_CV_C defect, the two C-dangling bonds relax inward and form a 5-membered ring, with a C—C separation of ≈1.7 Å in the bulk regime (Figure 3e,f). The C—C separation decreases as the surface is approached to a minimum C—C separation of 1.5 Å. The C_5N ring shows only marginal geometry changes as the surface is approached. In the bulk regime, the C—N bond length is 1.33 Å and the C—C bond length 1.41 Å (Figure 4b and Figure S12 and Table S3 (Supporting Information)), with no deviation observed between the perpendicular and tilted variants. In the near surface region, the previously described trends for the perpendicular and tilted variants are observed. A symmetric extension of the bonds in the direction of the surface is observed in the perpendicular case. The C—C extension in the C_5N rings is very small ≈0.01 Å, whereas the C_5 ring shows a more pronounced extension (0.04 Å), as the C—C bonds attempt to equalize the strain around the C_5 ring (Figure 4b). The tilted configuration shows an extension of the bonds in the direction of the surface, which has a negligible effect on the C—N bonds, with an extension of <0.01 Å, the C_5N C—C bonds show a similarly small extension of ≈0.02 Å (Figure 4b and Figure S12 and Table S3 (Supporting Information)). The impact of the surface is observed in the C_5 ring with an extension of ≈0.05 Å. It should be noted that the presence of the surface is only partly responsible, as the main driver for this extension is to equilibrate the C—C bonds around the C_5 ring, the presence of the surface provides the structural flexibility to achieve this.

2.3. Oxygen Defects

Oxygen-containing defects are prevalent in HC anodes, and can play an important role in increasing the surface wettability, which in turn improves the battery stability and performance.[1,7,15,36,39,62–65] Tuning the oxygen defect concentration and position (surface vs bulk) allows for physicochemical properties to be optimized.[1,62,64] Experimental XPS measurements commonly identify an oxygen content of ≈4% in HC, soft carbon, and composite carbon anodes for LIBs, NIBs, and KIBs.[66,67] Here, we consider four oxygen defects: single substitutional oxygen defect (O_C), oxygen substitutional defect and carbon vacancy (O_CV_C), double oxygen substitutional defect ($2O_C$), and triple oxygen substitutional defect ($3O_C$). The O_C and $2O_C$ defects are purely substitutional in nature, whereas the O_CV_C defect includes a carbon vacancy. The $3O_C$ defect

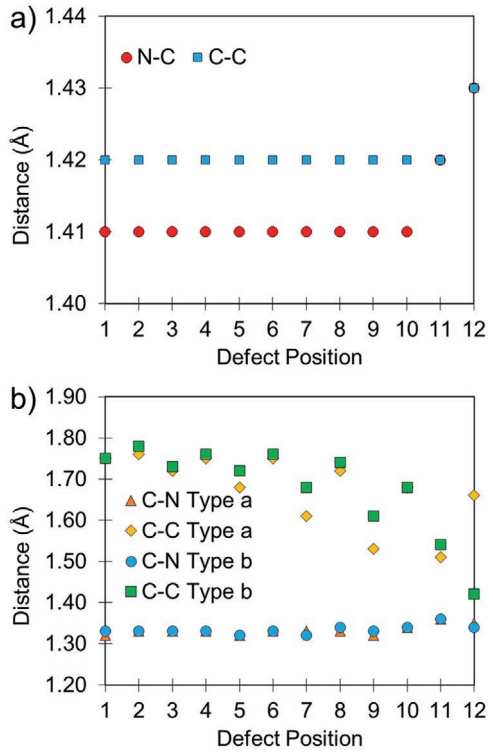

Figure 4. Interatomic distances as a function of defect position of a) the N_C defect and b) the N_CV_C defect. Interatomic distances for the optimized structures of these defects are included in Figure S8 and Table S2 (Supporting Information) for the N_C defect, Figures S10–S12 and Table S3 (Supporting Information) for the N_CV_C defect.

can be considered in two ways, either as a V_C with the C-dangling bonds substituted by 2-coordinated O-atoms, removing any unsaturated bonds from the systems, and with them any vacancy-like artefacts. Alternatively, the defect can be viewed purely in substitutional terms with three neighboring C-atoms substituted by O removing the central C-site in the process. Out of the two options, which is the most appropriate depends upon the mechanism of formation/oxidation, and the stage of growth at which the defects are introduced. Direct consideration of which is beyond the scope of this work, but it is important to note the varying ways of viewing the same defect, as in V_C terms this represents a passivated defect center, whereas in substitutional terms it would not. The calculated E_f^{defect} and optimized structures for the lowest energy configurations are presented in **Figure 5**a–d for each oxygen defect. For all the oxygen defects, distinct regimes are present; one bulk-like where there is little or no influence from the presence of the surface (blue in Figure 5a–d), and the near surface (green in Figure 5a–d) and surface (violet in Figure 5a–d) where the effect on the E_f^{defect} is far more pronounced.

The O_C defect shares features of both the V_C and the N_C defects, and its calculated E_f^{defect} (Figure 5a) are spread within a narrow range of 0.1 eV in the bulk regime (positions 1–8), with a gradual decrease in E_f^{defect} as the surface is approached. The lower E_f^{defect} at the surface defect sites are a result of strain in the direction of the surface elongating one of the C—O bonds, while being balanced by the gradual expansion of the lattice in the direction of the surface (**Figure 6**a,b). This trend continues until defect position 10, when the elongated C—O bond breaks and produces the 2-coordinated O and the C-dangling bond configuration (as observed at defect site 12 in Figure 5e). The accommodation of this is facilitated by the disruption of the π-system in the near surface regime and the favorable incorporation of the 2-coordinated O-center. These factors energetically compensate for the formation of the C-dangling bond and reduce the number of O-electrons in π^*-states. In common with the V_C defect, the dramatic decrease in E_f^{defect} (–1.9 eV) would be suggestive of an increased defect concentration in the surface and near surface regions (with the caveats highlighted above) with respect to the bulk (Figures S1d and S4, Supporting Information). While the magnitude of the drop in E_f^{defect} is larger for V_C, the absolute E_f^{defect} is 0.02 eV, which is much lower than 3.24 eV for the V_C at the same position. This suggests that at these chemical potentials, the HC surface is unstable to oxidation, in good agreement with experiment,[7,36] and one of the vectors of surface oxidation could be expected to occur via the formation of the O_C.

The E_f^{defect} for the O_CV_C defect (Figure 5b) in the bulk-like region sit within a tight energy range (≈0.2 eV), and a dramatic decrease in E_f^{defect} as the defect moves from the bulk to the surface (≈3.0 eV) is observed. Figure 5b shows the same cross trends as seen for N_CV_C that can be deconvoluted by defect configuration, as shown in the labeled subplots in Figure S14 (Supporting Information). What is interesting for the O_CV_C defect in contrast to the other considered here, is that the tilted defect configuration at the position directly below the surface is the lowest energy configuration (position 11, as shown in Figure 5f). In this defect position, both portions of the defect are accommodated with minimal strain, with the 5-membered ring showing negligible distortion, resulting in five equivalent C—C bonds (1.46 ± 0.03 Å) (Figure 6c,d). The C_5O ring likewise is incorporated with little distortion (<0.01 Å deviation). In general, a greater O_CV_C concentration would be expected in the near surface and surface regimes (Figures S1e and S4, Supporting Information). The exception to the general trend is position 11, as described above, the formation energy is E_f^{defect} = –0.33 eV at these chemical potentials, which in common with the other oxygen defects suggest that HC is unstable to oxygen.

For the $2O_C$ defect (Figure 5c), the bulk-like region can be seen to show a slight decrease in energy with a reduction of 0.25 eV between defect positions 1–7. In the near surface regime, the decrease in E_f^{defect} is far more pronounced with ≈–2 eV reduction between positions 8 and 12. In the bulk-like regime, the E_f^{defect} for the $3O_C$ defect (Figure 5h) show a smaller gradual downtrend, 0.17 eV from positions 1 to 7, but is energetically more stable than all the other oxygen defects. Approaching the surface, the energy decrease from positions 8 to 13 is 2.5 eV. The negative E_f^{defect} confirms that these oxygen-containing defects are energetically probable, in agreement with the experimental observations[7,15,39] and can be understood with reference to the substitutional oxidation of HC. Initially, a single O replaces a C-atom, producing the O_C defect and a C-dangling bond, this dangling bond can then be oxidized to form CO/CO_2[23] introducing a second C during an intermediate step. This leaves O in its preferred 2-coordinated configuration with no dangling bonds, and confirms that at these chemical potentials,

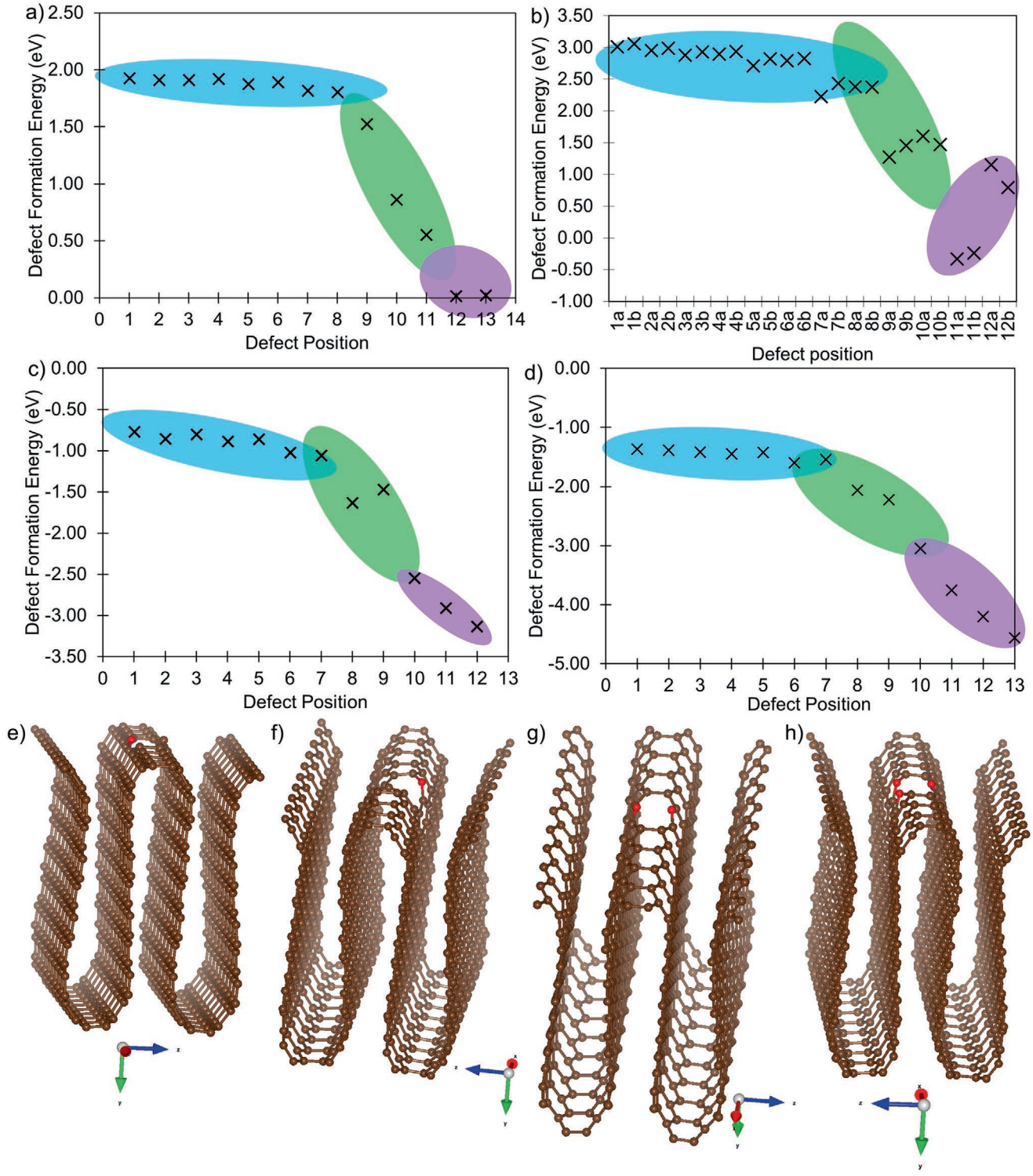

Figure 5. Defect formation energies for the oxygen defects at different lattice positions for the a) O_C, b) O_CV_C, c) $2O_C$, and d) $3O_C$ defects. The blue, green, and purple ovals indicate bulk, near surface, and surface positions, as specified in Figure 1. e) Optimized O_C defect at defect site 12 structure, f) optimized O_CV_C defect at defect site 11a structure, g) optimized $2O_C$ defect at defect site 12 structure, and h) optimized $3O_C$ defect at defect site 13 structure. Carbon atoms are brown spheres, and red oxygen.

the HC surface is prone to both oxygen heteroatoms and oxygen vacancy defects. From experimental evidence, oxygen heteroatoms are beneficial for improving the wettability of HC, and oxygen defects can enhance metal adsorption.[1,7,39,62–65]

In the bulk-like regime, the O_C defects sit at a three coordinated C-lattice site (Figures 5a and 6a, positions 1–9, and Figure S13 (Supporting Information)). As the surface is approached, the C—O bond perpendicular to the surface breaks

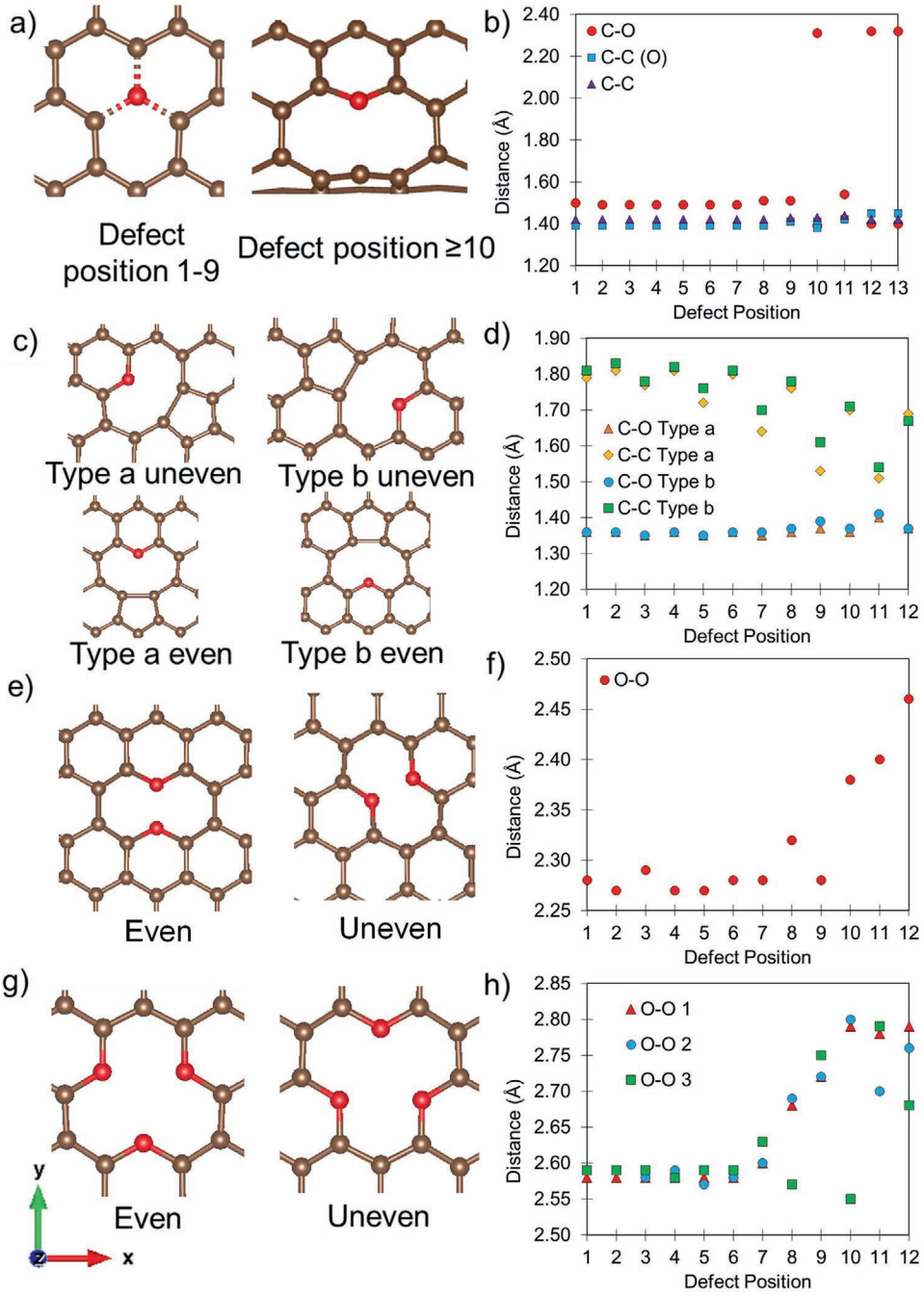

Figure 6. Inequivalent defect configurations (figures taken from the optimized bulk defect positions for easier graphical depiction, without the effect of curvature) for the oxygen defects and interatomic distances. a) The different O_C defect configurations at defect positions 1–9, and defect positions 10–13 where a larger elongation of the C—O bond is observed due to the surface curvature, b) the interatomic distances as a function of O_C defect location (C—C refers to the C—C bond next to the defect but not bonded to the O, C—C(O) refers to the C—C bond where one of the Cs are bonded to the O_C defect in the C—O distance), c) the different O_CV_C defect configurations at uneven defect positions configuration, d) the interatomic distances as a function of O_CV_C defect location (C—C refers to the shortest C—C bond in the 5-membered rings), e) different defect configurations for the $2O_C$ defect position configuration, f) the interatomic distances as a function of the $2O_C$ defect location (C—C refers to the shortest C—C bond in the 5-membered rings), g) the $3O_C$ defect configurations, and h) the O—O interatomic distances as a function of defect location (C—C refers to the shortest C—C bond in the 5-membered rings). Carbon atoms are brown spheres, and red oxygen. Interatomic distances for the optimized structures of these defects are included in Table S4 (Supporting Information) for the O_C defect, Figure S17 and Table S5 (Supporting Information) for the O_CV_C defect, Figure S19 and Table S6 (Supporting Information) for the $2O_C$ defect, and Figure S21 and Table S7 (Supporting Information) for the $3O_C$ defect.

(Figure 6a), leaving a C-dangling bond. In the bulk-like region, there is a more marked distortion in the lattice than was observed for the N_C defect at the same positions (Figure 6b and Table S4 (Supporting Information)). The C—O bond lengths are

1.49–1.50 Å, representing a 6% extension with respect to the C—C bonds. To accommodate this expansion, the next neighboring C—C bonds are contracted by 0.03 Å (2%), after which the bulk C—C bond length (1.42 Å) is recovered (C—C (O) in Figure 6b). As the defect approaches the surface (Figures 5c and 6a,b positions 7–9), the threefold symmetry with equal C—O bond length is distorted as the C—O perpendicular to the surface begins to extend. This extension results in the breaking of the perpendicular C—O bond, positions 10–13, resulting in a 2-coordinated O and a C-dangling bond (Figure 6a). The 2-coordinated C—O bond is significantly shorter (1.39–1.40 Å) with the broken C—O bond relaxing outward to a separation of ≈2.35 Å (Figure 6b). The surface positions result in a rupture of the bond linking the two graphene sheets, resulting in a C-dangling bond projecting from one of the sheets, and an O-capping of the other.

The structural properties of the O_CV_C defect are similar to the V_C defect as it relaxes to give a 5-membered C ring, the C-dangling bond of the V_C is replaced by the 2-coordinated O-capped C_5O ring, leaving no unsaturated bonds in the defect (Figure 6c and Figures S10 and S11 (Supporting Information)). Geometrically, the 5-membered ring is more easily accommodated in the O_CV_C than the V_C with a C—C separation of ≈1.8 Å (for V_C ≈ 2.0 Å) in the bulk, which decreases to ≈1.5 Å at the surface, as observed for the V_C defect (Figure 6d and Figure S17 and Table S5 (Supporting Information)). As there are no unsaturated bonds in the system, the cross-linking observed for the V_C at strained edges is not seen in the O_CV_C defect case. In common with the N_CV_C defect, there are both perpendicular and tilted variants (Figure 6c), with the same a or b type configurations where the O is positioned at the top or bottom site, respectively. For the a and b type perpendicular configurations, there are no significant distortions in the bulk regime (Figure 6d), whereas a small stretching of the bonds in the direction of the surface in the near surface regime is observed (Figure S17 and Table S5, Supporting Information).

The $2O_C$ defect is made up of two O_C defects sitting at neighboring sites, with an O—O separation of ≈2.3 Å in the bulk-like regime, which increases as the surface is approached to give a maximum O—O separation of ≈2.5 Å when the defect is directly at the surface (Figure 6e,f and Figures S18 and S19 and Table S6 (Supporting Information)). For the $2O_C$ defect, two configurations are possible with the defect sitting perpendicular to the surface (Figure 6e even), or at a 60° angle with respect to the surface (Figure 6e uneven). In the bulk context, the defect has twofold symmetry with each C_5O ring equivalent. In the perpendicular case, all C—O and C—C bonds form equivalent pairs (no distortion within the C_5O rings observed due to position of a given atom with respect to the surface). The C—O bonds show no distortion and a negligible extension (0.01 Å) as the defect is moved from the bulk to the surface (Figure 6f and Table S6 (Supporting Information)). The C—C bonds perpendicular to the surface show a similar small extension (0.01 Å) as the surface is approached. A greater relaxation is seen for the final pair of C—C bonds opposite the C—O, as the surface is approached (Figure 6f) and the O—O separation increases the C—O—C flattening with the O sitting of opposite sides of the graphene sheet (defect position 12, Figure S18, Supporting Information), which necessitates the extension of the C—C bonds to accommodate (≈2%). This further reduces the E_f^{defect} for the $2O_C$ defect at the surface. For the tilted configuration, the picture is more complex as the bond pairs within a C_5O ring become inequivalent as the surface is approached (Figure 6f). In the bulk context uneven numbers (positions 1–7 Figures 5c and 6f), there is no meaningful impact from the presence of the surface and the defect is symmetric, with twofold symmetry as described above. In the near surface and surface regimes, distortions break the symmetry of the defect as the bonds (C—O and C—C) closer to the surface extend by 1–3% depending upon position.

The $3O_C$ defect has threefold symmetry with three equivalent O-atoms, the O—O separation is 2.58 Å, with C—O bond lengths of 1.38 Å (Figure 6g,h). In common with the other defects considered here, as the $3O_C$ is moved toward to the surface, there is an elongation of the bonds perpendicular to the surface (Figure 6h and Figure S20 (Supporting Information)). The O—O separation extends to 2.78 Å (2.68 Å for the in-plane O), and the C—O bonds become inequivalent with the bond perpendicular to the surface showing a small extension (≈0.02 Å) to 1.41 Å, which is compensated for by an equivalent contraction in the neighboring C—C bonds of the C_5O ring (Figure S21 and Table S7, Supporting Information).

2.4. Nitrogen and Oxygen Defects

From the analysis above, both oxygen and nitrogen defects (or dopants) are expected to be present from their generally low E_f^{defect}. From experimental evidence, it has also been observed that extrinsic oxygen defects can arise as a consequence of nitrogen doping.[68] In this section, we investigate two nitrogen- and oxygen-containing defects, the N_CO_C and N_C2O_C defects (**Figure 7**). These defects are geometrically similar to the $2O_C$ and $3O_C$ defects, respectively. The number of possible configurations for the N_CO_C defect case increases significantly as compared to the previously discussed defects. In common with the $2O_C$ defect, the N_CO_C defect can sit either perpendicular or tilted with respect to the surface. Additionally, either N (type a) or O (type b) can sit closest to the surface (Figure 7c). This in effect breaks the twofold symmetry that was present for the $2O_C$ defect and requires each configuration to be considered explicitly. The N_C2O_C defect represents a variation of the $3O_C$ where one of the O (which was originally a C atom) atoms has been replaced by N. In the same way as the $3O_C$, this can be viewed as being a purely substitutional defect or based upon a pre-existing V_C. The introduction of the N-atom breaks the threefold bulk symmetry of the $3O_C$ (in a similar way to N_CO_C vs $2O_C$) while shifting the principal symmetry axis from perpendicular to in the plane of the graphene sheet (Figure 7d).

The E_f^{defect} of the N_CO_C defect at different positions and configurations are shown in Figure 7a. While the bulk and surface regimes seen for the $2O_C$ defect are present, the distribution of energies is broader with a number of cross trends. To understand these trends, it is instructive to deconvolute the E_f^{defect} for the different defect configurations outlined above and shown in Figure 7c and Figure S22 (Supporting Information). The energetic differences of these become more pronounced as the surface is approached, with the symmetric even geometry

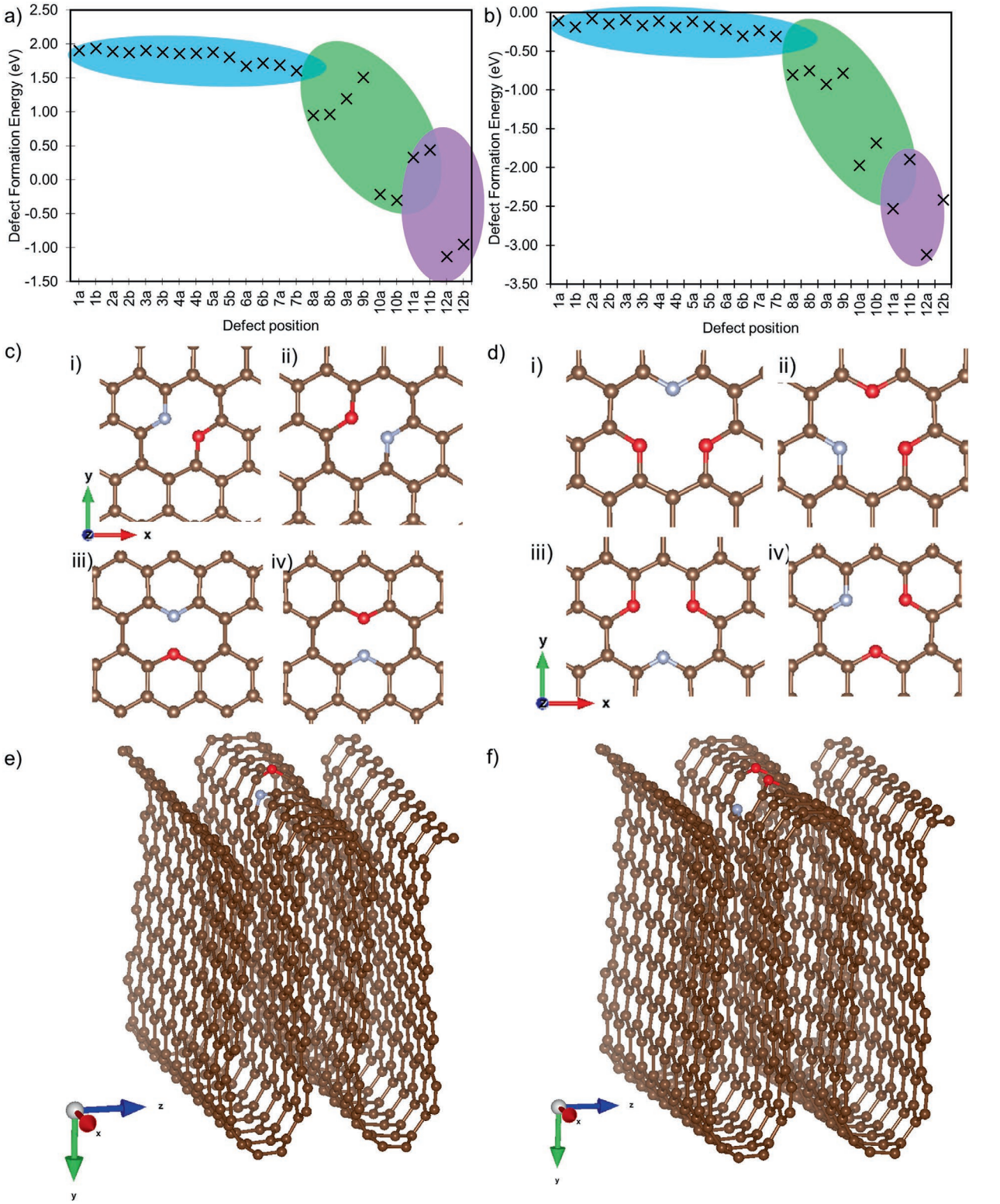

Figure 7. Defect formation energies at different lattice positions for the a) N_CO_C and b) N_C2O_C defects. The blue, green, and purple ovals indicate bulk, near surface, and surface positions, as specified in Figure 1. c) The inequivalent N_CO_C defect configurations where i) is the type a at uneven defect position configuration, ii) type b at uneven defect position configuration, iii) type a at even defect position configuration, and iv) type b at even defect position configuration in (a). d) The inequivalent N_C2O_C defect configurations where i) is the type a at uneven defect position configuration, ii) type b at uneven defect position configuration, iii) type a at even defect position configuration, and iv) type b at even defect position configuration in (b). The optimized structure of the defects at position 11a are shown in e) for N_CO_C and f) for N_C2O_C as an example. All optimized structures of these defects are included in Figures S23, S24, S27, and S28 (Supporting Information). Carbon atoms are brown spheres, gray nitrogen, and red oxygen.

lower in energy than in its tilted counterpart at a given depth (Figure 7c and Figure S22 (Supporting Information)). The E_f^{defect} for the surface defects give support to the experimental observations that edges are susceptible to nitridation in a similar manner to oxidation, with sites at defect position 10 and above giving negative E_f^{defect} at these chemical potentials. In contrast to the $2O_C$ defect, there is a strong location dependence, with the negative E_f^{defect} only found in the surface and near surface regimes (Figures S1h and S5, Supporting Information).

The distinct E_f^{defect} profile is also clearly visible for N_C2O_C (Figure 7b). Defect positions 1–7 show the gradual decrease in E_f^{defect} typical of the bulk-like regime, while defect positions 8–12 show the more dramatic decrease in E_f^{defect} associated with the surface. The bulk energies show a shallow decrease of only 0.1 eV, with 2.9 eV reduction in the surface regime. The same cross trends previously described and due to the presence of the defect configurations shown in Figure 7d give rise to this and can be deconvoluted by separating the configurations (Figure S26, Supporting Information). There is a hint of a secondary trend along the lines of the uneven–even effect previously described, that can be ascribed to the direction of the defect (Figure 7d), although it is important to note that the energy changes here are very small (ΔE_f = 0.04 eV) and not as significant as those observed for N_CO_C.

For the optimized N_CO_C structures, the N and O atoms deviate from the graphene plane (Figures S23 and S24, Supporting Information), with the lowest energy configuration placing them on opposite sides of the C-sheet (Figure 7e). The bulk-like configuration has a N—O separation of ≈2.3 Å in both arrangements (**Figure 8**a). The N—C bond is ≈4% shorter than the N—O, incorporated into the lattice with no appreciable distortion, and is less susceptible to any deviations as the surface is approached (Figure 8a). For the C_5N and C_5O units in the perpendicular variant, the bonds are symmetric, forming equivalent pairs as with the $2O_C$. The tilted variant shows small extensions of the bonding in the direction of the surface (after position 8 in Figure 8a and Figures S23 and S24 (Supporting Information)). In the bulk regime, there is no geometric distinction between the type a and b configurations (Figure 8a and Figure S25 and Table S8 (Supporting Information)), with the absolute location and perpendicular versus tilted configuration being better predictors of the geometric distortions.

Examining the geometric structure of the N_C2O_C defect in the bulk-like regime, the different defect configurations are geometrically equivalent (Figure 8b), with an O—O separation of 2.60 Å and a N—O separation of 2.58 Å. The C—N bond is 1.34 Å in common with the other 2-coordinated N-centered defects described here. Likewise, the C—O bond is 1.38 Å, again in agreement with the other 2-coordinated O-defects (Figure S29 and Table S9, Supporting Information). In common with the other defects presented here, as the surface is approached, the bonds perpendicular to the surface extend (Figure 8b), with the O—O separation increasing to 2.9 Å at the surface, while the N—O increases to 2.65 Å at the same position (12). The changes in the N—O and C—O bonds are far less pronounced at 0.01 and 0.03 Å, respectively. These extensions are accommodated by matching contractions in the C—C bonds of the C_5O/C_5N rings (Figure 8b).

For the nine defects considered in this work, it is clear that the E_f^{defect} decreases as the defects are moved toward the surface. Inspecting the defect formation energies at the different sites, the defects in positions 1–7 (bulk-like) show similar E_f^{defect}. These E_f^{defect} then gradually decrease through the near surface region to finally reaching the minimum at the surface defect positions. The exception to this trend is the N_C defect, which shows little change in E_f^{defect} as a function of position due to it being easily accommodated at the C-lattice site with negligible deviation. These results accord well with the experimental observations, describing an increased defect concentration at the edge sites, along with the observed instability to oxidation that is well-known for HC materials.[1,7,39,62,69] The results presented here allow an understanding of the relative defect concentrations between the bulk and the surface to be understood, along with absolute defect concentrations and defect probability distributions in the case of samples that have reached thermodynamic equilibrium (or that it is a reasonable assumption to make). Hence, it is of importance to not only consider defects on planar motifs (such as graphene and the basal plane as we have considered previously) but also on curved morphologies and surfaces to optimize material performance.

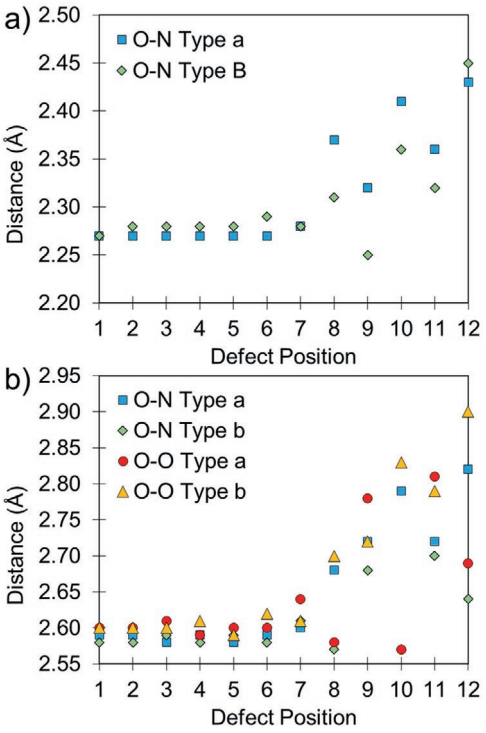

Figure 8. Interatomic distances in optimized defect structures for a) the N_CO_C and b) the N_C2O_C defects at different lattice positions. Type a and b refers to the inequivalent defect configurations presented in Figure 7c,d. Interatomic distances for the optimized structures of these defects are included in Figure S25 and Table S8 (Supporting Information) for the N_CO_C defect, and Figure S29 and Table S9 (Supporting Information) for the N_C2O_C defect.

2.5. Adsorption of Li, Na, and K on V_C, N_C, and O_C Defects

During electrochemical cycling of HC anodes, the metal incorporation can follow different mechanisms depending on carbon morphology, alkali metal cation, and site saturation. A

lot of debate remains in the literature about the HC charge/discharge mechanism. Initially, the so-called "falling cards model" was introduced by Stevens and Dahn[4] for Na^+ storage in HC. Following this model, the initial sodiation (sloping region) was attributed to Na^+ intercalation in the graphitic stacks, whereas the low voltage plateau region was attributed to Na^+ storage in nanopores. In recent years, this initial model has been extended and refined, also taking into account the effect of heteroatoms and the fact that not all HCs have the same atomic structure.[9,68,70–73] Subsequent studies suggested that the sloping region could also be due to metal ion adsorption, and bonding to carbon vacancies.[7,33,39,65] In general, intercalation, carbon vacancy adsorption, heteroatom site adsorption, and pore filling have all been proposed to contribute to the charge/discharge mechanisms for the HC anode materials.[7,33,39,65] In situ TEM studies showed that the initial sodiation of a HC anode occurs through surface active site adsorption, followed by intercalation into the graphitic layers.[50] The surface adsorption can also be followed by studying the anode expansion, due to the lower volume expansion associated with adsorption when compared to intercalation.[36,50] The volumetric change of a HC NIB anode was studied by Wang et al. showing that the initial sodiation process took place mainly through surface adsorption (due to the stable volume), whereas intercalation occurred after 300 s where there was a sharp rise in volume.[50] In situ electrochemical dilatometry further confirmed that the anode thickness changes as a function of sodiation time, and is further dependent on the microstructure, pyrolysis temperature, and heteroatom concentration of the HC material.[36] The surface of the anode has been shown to be important, with surface defects (especially when there is a significant oxygen concentration identified from XPS measurements) responsible for providing additional initial metal ion storage sites, and irreversible metal trapping.[7,38,39,74] The effect of surface, interlayer distance, pore size, carbon morphology, defects, and heteroatoms will be dependent on pyrolysis/carbonization temperature (with less surface area, fewer defects, and more graphitic character observed with increasing pyrolysis temperature) and the initial reagents (where oxygen and nitrogen dopants can be introduced to tune material properties).[21,27,36,39,75] Additionally, the main contribution to Li storage in HC comes from intercalation, with initial contribution from surface adsorption as confirmed by in situ Raman analysis of Li in HCs.[33,65,76–79] For KIBs, the graphitic stacks' interlayer distances accessible to Na^+ and Li^+ storage can be inaccessible, with greater interlayer distances required.[33,61,66,80] Previously, we have studied, in isolation, basal plane defect adsorption, and intercalation in planar graphitic pores with varying interlayer distances (c) as guided by experimental HC characterization.[33,34] From these studies, we showed that metal adsorption is greatly enhanced at defect sites,[34] and that especially the sodium and potassium intercalation is heavily dependent on c, with potassium showing energetically favorable intercalation energies (i.e., negative binding energies) first at $c > 3.85$ Å, and sodium at $c > 3.49$ Å.[33] The latter were further confirmed by muon spin rotation spectroscopy.[21] Employing the simulation model described herein, the effect of curvature, graphitic stack interlayer, and defect location on metal adsorption will be explored. This gives important insight adding to the previous knowledge of metal adsorption on defective planar basal plane surfaces, metal intercalation in nondefective graphitic stacks, and metal adsorption on curved motifs.[33,34] Inspecting the binding energy of Li, Na, and K in between planar graphitic layers as a function of c as presented in our previous work[33] at c between 3.3 and 4.0 Å, the metal binding energy as a function of c decreases near linearly. As c increases, Li, Na, and K shift from intercalation to surface adsorption and converge to the graphene metal adsorption energies.[33,34] Performing a linear regression (Figure S30, Supporting Information) shows that the increase in energy for each Å (in this range of c) is 6.5 eV for K, 2.7 eV for Na, and much lower for Li at 0.59 eV, as Li from the simulated binding energies shows energetically favorable intercalation at all investigated c. Here, we extend our previous studies to investigate how these trends are impacted by the addition of simple point defects (carbon vacancies, oxygen, and nitrogen heteroatoms), to gain insight into the surface adsorption and intercalation mechanisms. The metal adsorption energy (E_{ads}) at different defect positions was calculated according to Equation (2)

$$E_{ads} = E_{Metal-Defective} - \mu_{Metal} - E_{Defective} \quad (2)$$

Here, $E_{Metal\text{-}Defective}$ is the total energy of the defective system with an added metal atom, and μ_{Metal} is the chemical potential of the metal species. The chemical potential of the metal is here taken as the total energy of a single metal ion in a vacuum cell (20 Å × 20 Å × 20 Å).[7,33,34] Hence, the more negative the E_{ads}, the stronger the adsorption of the metal to the carbon system. The resulting adsorption energies are plotted in **Figure 9** as a function of defect position (Figure 1), with optimized structures included in the Supporting Information. From Figure 9, it is clear that in agreement with the previously observed trends for both intercalation and surface adsorption, Li, Na, and K behave differently. Hence, we will first discuss the metals on the defect systems individually, and then summarize the intermetal trends separately.

Li shows the strongest interaction with the V_C containing carbon lattice (as seen from the most negative adsorption energies in Figure 9a). For this system, Li shows similar adsorption strengths at the bulk-like vacancies (defect positions 1–4) and on the surface vacancies (defect positions 9–12). Comparing the energies at defect positions 1–8, i.e., the intercalation-like region, the Li intercalation energies are much improved as compared to Li intercalation in pristine planar graphitic layers. The Li adsorption energies for V_C at defect positions 5–8 are weaker, signifying a transition from surface adsorption to intercalation, where it can be expected that the mechanisms compete. The optimized structures of Li and the V_C defects are included in Figure S31 (Supporting Information). The transition (in terms of Li adsorption energies) between the intercalation and surface adsorption behavior is not as clear for the N_C and O_C defect containing systems. For the N_C defect (Figure S32, Supporting Information), the Li adsorption energies remain flat with defect position, with the strongest adsorption obtained at the surface. Li at defect position 12 shows a 0.7 eV stronger adsorption energy than for Li intercalation at the bulk defect positions. The O_C defect shows stronger Li adsorption from defect sites 9–12 where the O_C defect opens up the hexagonal units at the strained surface (Figure S33, Supporting Information). The

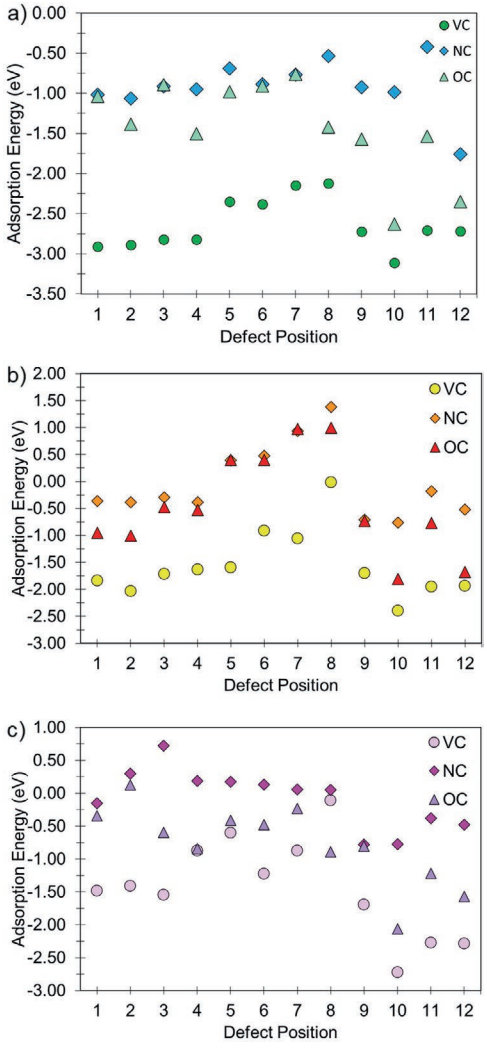

Figure 9. Metal adsorption energies for a) Li, b) Na, and c) K in the V_C, N_C, and O_C defect systems.

same effect is only observed for Li at defect site 12 in the N_C containing system. At defect site 12, the adsorption of Li causes the hexagonal units at the curved surface to break, with the C—N distance extending from 1.43 to 2.23 Å upon Li adsorption (Figure S32, Supporting Information).

For Na, three clear trends are observed for each defect in Figure 9b. In defect positions 1–5, Na is intercalated, and at positions 9–12 adsorbed on the surface. Only for Na at V_C defect (Figure S34, Supporting Information) sites is the sites (and hence transition) between these regimes energetically favorable, although at a very weak adsorption energy (–0.02 eV). This furthers the analysis seen above for Li adsorption, that carbon vacancy defects are highly favorable for metal intercalation. For Na at defect sites 6–8, the Na adsorption energy is positive for both the N_C and O_C systems. These are the narrowest sites, agreeing with our previous results of Na intercalation in graphitic stacks, with Na intercalation becoming energetically favorable at $c = 3.49$ Å. The V_C defect induces distortions to the carbon lattice, expanding the interlayer distance locally to 4 Å, allowing Na to intercalate. The same structural distortion is observed for Na at N_C and O_C defect site 8 (Figures S35 and S36, Supporting Information), but the energetic cost for this distortion is higher, resulting in positive adsorption energies. Combining the knowledge gained above that surface defects have lower defect formation energies, and hence expected to be present in higher concentrations under equilibrium conditions, with the strong Na adsorption energies at the surface defect sites, these results suggest that for sodiation, surface adsorption at curved surface lattice sites forms an important part of the sodiation mechanism. As a general rule, the simulated adsorption (or binding) energies can be directly compared to cell voltage (V) assuming $V = (-E_{ads})$. The cutoff voltage for NIB HC anodes is typically 2 V versus Na^+/Na, which means that any E_{ads} stronger than −2 eV could lead to metal trapping, leading to irreversible capacity loss.[7,15] To this end, the V_C and O_C surface defects would be expected from these simulations to lead to irreversible capacity loss. Experimental studies have tested to what extent the cell voltage cutoff affects the cycling performance of Na/HC half cells.[15] Charging the half-cell (made of HC anode containing significant oxygen concentrations and defects) to 3 V for a duration of 2 h led to the release of an additional 100 mAh g^{-1} specific capacity, suggesting that for HC anodes, careful tuning and employment of cutoff voltage may be necessary when they contain these defects.[15]

For K adsorption (Figure 9c), the picture is more complicated. For the V_C and O_C defect containing systems, K adsorption energies are negative, with V_C showing the strongest K adsorption. As opposed to Na and Li, K remains in the bulk (as described in Figure 1) in the systems with these defects at all defect sites except 9–12 (Figures S37–S39, Supporting Information). Hence, discussing the K adsorption as a function of interlayer distance is for K disingenuous as K remains at the wider interlayer distances. The weak K adsorption energies are further due to the high structural distortions (especially in the N_C- and O_C-containing systems) induced by the metal. For defect sites 9–11 (which show the strongest K adsorption energies in Figure 9c), K adsorbs above the interlayer space. Inspecting the optimized structures for K in the systems with V_C and O_C at defect site 10 (with both the strongest K adsorption), K in both these sites interacts with a dangling carbon bond at the strained lattice site (Figures S37 and S39, Supporting Information). Hence, it can be deduced that these defect sites are particularly important for potassiation, as well as sodiation. This dangling bond is not opened up by the N_C defects (Figure S38, Supporting Information), hence not giving the same enhancement to the K adsorption.

From the above analysis, it is clear that both O_C and N_C defects enhance the metal surface adsorption, but that the V_C defect leads to the strongest intercalation and surface interactions with all the metals. Generally, as discussed previously,[33,34] the energetic ordering of Li, Na, and K is different in the intercalation regime ($E_{ads,\,Li} < E_{ads,\,Na} < E_{ads,\,K}$) than in the adsorption regime ($E_{ads,\,Li} < E_{ads,\,K} < E_{ads,\,Na}$). This ordering, with Na having stronger interaction with the carbon lattice when in the intercalated regime than K, is due to the larger ionic size of K.[33] K is also the only metal that does not break the sp^3-hybridized carbon interconnect formed when adding a V_C defect to lattice site 8. The Na sits within an interlayer distance of 4 Å, and Li 3.78 Å, both at the defect site, whereas K remains in the bulk

regime 7.89 Å away from the sp^3 interlink and the defect site, remaining close to site 1, as defined in Figure 1. Hence, it would be expected that in NIBs, and LIBs, these kinds of sp^3 interlinks would be broken during lithiation and sodiation. For the metals at defect sites 9 and 10, the metals sit above the gap between the carbon sheets. This corresponds to the initial intercalation step. At defect sites 11–13, the metals are adsorbed at the surface. Both Li and K sit closest to the carbon surface (1.03 Å for Li, and 1.12 Å for K) at defect position 13, whereas Na is the closest when V_C is at position 11 (1.25 Å). Na adsorbed at V_C at site 10 is also the strongest adsorption site for Na, and binds stronger to the surface than K at this site. For Li, no clear preference can be seen for intercalation or surface adsorption, indicating that both these will be equally important in the lithiation mechanism. This is in agreement with previous experimental studies of the lithiation mechanism of HC and other carbon anodes such as graphite. Cell tests comparing the same HC materials for LIBs, NIBs, and KIBs were conducted in a previous publication.[33] The study utilized a series of HC materials synthesized by hydrothermal carbonization from glucose (containing oxygen heteroatom defects, but no traceable amount of nitrogen from XPS analysis) and pyrolysis at different carbonization temperatures. From the charge–discharge curves of the HC materials with the most graphitic character (narrowest interlayer distances at 3.5–3.6 Å, respectively, and the lowest oxygen concentration), it could be observed that both the Li and Na cells exhibited higher specific capacities than the K cells due to the hindrance of the K^+ ions to intercalate in the smaller interlayer distances (as observed in Figure 9c). Comparing the Li and Na capacity showed that Li had higher specific capacities than Na, agreeing with the trend presented in this work (Figure 9a,b). For the HC materials carbonized at lower temperature with wider interlayer distances (>3.7 Å), the lithiation remained more favorable with higher capacities than both sodiation and potassiation (with the sodiation and potassiation showing similar behavior). This agrees with our analysis that the interlayer distance and defect location have larger impact on the metal incorporation than the type of defect does. The HC materials carbonized at lower temperature also showed more sloping region capacity, which is typically coupled to metal adsorption at defect sites as well as intercalation. This indicates that the presence of defects does lead to higher metal storage (by opening up additional surface adsorption sites), in agreement with our DFT simulations. For optimum performance, there needs to be a balance between accessible bulk intercalation sites, surface defect sites for the initial metal adsorption, and that the defects should not bind the metals too strongly as to hinder the further metal incorporation mechanisms.

From these results, it is clear that Li is the least sensitive to the layer separation and shows little deviation between the intercalation and adsorption regimes. Intercalation becomes less favorable in the near surface region as a result of the reduced layer separation. The energy penalty accords well with the previous defect free study,[33] with the absolute binding energy dictated by the defect type. In the case of Na, the picture is more complex as a result of its larger ionic radius, and weaker binding, which combine to give a much greater sensitivity to layer separation. However, the same trends described for Li can be observed for Na, with the absolute magnitude of the adsorption energy dictated by the defect type. The greater sensitivity to layer separation leads to a much larger energy penalty in the near interface regime, in accordance with the defect free adsorption energy penalty as with Li. In the case of K, the picture becomes less clear as *c* for the HC characterized here is too narrow to favorably accommodate K. As a result, for K, no stable minima could be identified. This makes it impossible to comment on the energetic penalty due to layer separation for K in these models, although it is still possible to see the shift from intercalation (albeit lacking the *c* distribution) to adsorption.

3. Conclusion

In this paper, a systematic DFT study of the effect of defect location on defect formation in nanoporous carbon anode materials was conducted. The defects considered were based on carbon monovacancy, nitrogen substitutional heteroatom defects, oxygen substitutional heteroatom defects, and combinations of these. The defects were studied at different locations in three general lattice regions: bulk-like, near surface, and surface. From this analysis, a strong dependence of defect position was identified, with the defect formation energy dramatically increasing as the surface is approached (as compared to the bulk) due to the increased curvature and strain. To understand what contributions the defect location in respect to the carbon matrix interlayer distance, and surface have on the initial lithiation, sodiation, and potassiation mechanisms, we further calculated Li, Na, and K adsorption at the different single center defect sites. From these simulations, it was shown that the defect (at each defect site) that leads to the strongest metal adsorption is the carbon monovacancy. Furthermore, it was shown that surface adsorption is highly energetically favorable when the O_C defect at a strained lattice site leads to a dangling bond, and that careful consideration of the cell voltage would be an important engineering tool to minimize capacity loss due to metal trapping at high adsorption energy defect sites. However, the location of the defect, in terms of intercalation in varying interlayer distances and on surface, was of more importance than the defect. From these simulations, these surfaces have high defect concentrations and disorders, something that needs to be considered when studying both the lithiation/sodiation/potassiation mechanisms, and electrolyte anode interfaces.

Finally, defects can be both beneficial and detrimental to alkali metal ion battery performance. As shown from this and previous work,[7,34,36,81,82] defects can increase the adsorption of Li, Na, and K in these anode materials, both at the surface and in the bulk through intercalation, and thus would enhance the initial lithiation, sodiation, and potassiation, respectively. Heteroatom doping with O and N should be explored either by choosing reagents with high oxygen or nitrogen content when synthesizing these HC compounds, or by heat treatment in an oxidative environment. However, these strong metal adsorption energies at the defect sites could lead to metal trapping, limiting the cycling performance. Hence, from a material design perspective, defect engineering should be considered and explored as a route to

higher performance LIB, NIB, and KIB anodes, but it will be important to carefully tune the defects and their location to get the optimum performance.

4. Experimental Section

In this work, DFT simulations were used to systematically investigate the possible locations of a range of defects in the carbon lattice. All the DFT simulations were carried out using the CP2K code.[83–86] The Perdew-Burke-Ernzerhof functional was utilized with the TZVP-SR-MOLOPT basis sets, a 650 Ry cutoff, and all calculations were performed at the Γ-point with a minimum convergence criteria of 0.01 meV per formula unit.[84,87–89] This setup formed the basis for all the calculations, allowing for relaxation around the defect group site to be contained within the supercells and was also employed to study similar systems previously.[33] This allowed for a large enough simulation cell to reproduce the bulk graphite electronic structure at the center. The van der Waals interactions were accounted for by utilizing the DFT-D3 method with Becke–Johnson dampening in all simulations.[90–94] For all models, bulk cell optimizations were performed to fully relax the structure in terms of lattice parameters and ion positions, whereby the lattice parameters were kept fixed in the geometry optimizations for the defect studies. All figures of the atomic structures were made with VESTA.[95]

Supporting Information

Supporting Information is available from the Wiley Online Library or from the author.

Acknowledgements

The authors would like to thank the Engineering and Physical Sciences Research Council for funding (Grant No. EP/R021554/2). The authors are grateful to the UK Materials and Molecular Modelling Hub for computational resources, which is partially funded by EPSRC (Grant No. EP/P020194/1), and the Imperial College Research Computing Service, DOI:10.14469/hpc/2232.The authors would also like to acknowledge the use of Athena at HPC Midlands+, which was funded by the EPSRC under Grant No. EP/ P020232/1. The authors would like to thank the University of Surrey for access to its High Performance Computing facility and the Eureka HPC cluster.

Conflict of Interest

The authors declare no conflict of interest.

Data Availability Statement

Data available on request from the authors

Keywords

alkali ions, anodes, batteries, defects, graphitic carbon, hard carbon, heteroatoms

Received: December 4, 2020
Revised: February 10, 2021
Published online: March 18, 2021

[1] E. Irisarri, A. Ponrouch, M. R. Palacin, *J. Electrochem. Soc.* **2015**, *162*, A2476.
[2] D. Larcher, J. M. Tarascon, *Nat. Chem.* **2015**, *7*, 19.
[3] J. Deng, W.-B. Luo, S.-L. Chou, H.-K. Liu, S.-X. Dou, *Adv. Energy Mater.* **2018**, *8*, 1701428.
[4] D. A. Stevens, J. R. Dahn, *J. Electrochem. Soc.* **2000**, *147*, 1271.
[5] N. Yabuuchi, K. Kubota, M. Dahbi, S. Komaba, *Chem. Rev.* **2014**, *114*, 11636.
[6] R. A. Adams, A. Varma, V. G. Pol, *Adv. Energy Mater.* **2019**, *9*, 1900550.
[7] H. Au, H. Alptekin, A. C. S. Jensen, E. Olsson, C. A. O'Keefe, T. Smith, M. Crespo-Ribadeneyra, T. F. Headen, C. P. Grey, Q. Cai, A. J. Drew, M.-M. Titirici, *Energy Environ. Sci.* **2020**, *13*, 3469.
[8] K. L. Hong, L. Qie, R. Zeng, Z. Q. Yi, W. W. X. Zhang, D. Wang, W. Yin, C. Wu, Q. J. Fan, W. W. X. Zhang, Y. H. Huang, *J. Mater. Chem. A* **2014**, *2*, 12733.
[9] B. Xiao, T. Rojo, X. Li, *ChemSusChem* **2019**, *12*, 133.
[10] Q. Jin, K. Wang, P. Feng, Z. Zhang, S. Cheng, K. Jiang, *Energy Storage Mater.* **2020**, *27*, 43.
[11] X. Dou, I. Hasa, D. Saurel, C. Vaalma, L. Wu, D. Buchholz, D. Bresser, S. Komaba, S. Passerini, *Mater. Today* **2019**, *23*, 87.
[12] R. E. Franklin, *Acta Crystallogr.* **1951**, *4*, 253.
[13] D. A. Stevens, J. R. Dahn, *J. Electrochem. Soc.* **2000**, *147*, 4428.
[14] A. Hashimoto, K. Suenaga, A. Gloter, K. Urita, S. Iijima, *Nature* **2004**, *430*, 870.
[15] D. Sun, B. Luo, H. Wang, Y. Tang, X. Ji, L. Wang, *Nano Energy* **2019**, *64*, 103937.
[16] V. G. Pol, J. Wen, K. C. Lau, S. Callear, D. T. Bowron, C. K. Lin, S. A. Deshmukh, S. Sankaranarayanan, L. A. Curtiss, W. I. F. David, D. J. Miller, M. M. Thackeray, *Carbon* **2014**, *68*, 104.
[17] Q. Zhong, Q. Mao, L. Zhang, J. Xiang, J. Xiao, J. P. Mathews, *Carbon* **2018**, *129*, 790.
[18] D. Saurel, B. Orayech, B. Xiao, D. Carriazo, X. Li, T. Rojo, *Adv. Energy Mater.* **2018**, *8*, 1703268.
[19] V. V Ivanovskaya, A. Zobelli, P. Wagner, M. I. Heggie, P. R. Briddon, M. J. Rayson, C. P. Ewels, *Phys. Rev. Lett.* **2011**, *107*, 065502.
[20] C. Lechner, P. Baranek, H. Vach, *Carbon* **2018**, *127*, 437.
[21] A. C. S. Jensen, E. Olsson, H. Au, H. Alptekin, Z. Yang, S. Cottrell, K. Yokoyama, Q. Cai, M.-M. Titirici, A. J. Drew, *J. Mater. Chem. A* **2020**, *8*, 743.
[22] P. Bai, Y. He, X. Zou, X. Zhao, P. Xiong, Y. Xu, *Adv. Energy Mater.* **2018**, *8*, 1703217.
[23] A. Beda, C. Villevieille, P.-L. Taberna, P. Simon, C. M. Ghimbeu, *J. Mater. Chem. A* **2020**, *8*, 5558.
[24] X.-F. Luo, C.-H. Yang, Y.-Y. Peng, N.-W. Pu, M.-D. Ger, C.-T. Hsieh, J.-K. Chang, *J. Mater. Chem. A* **2015**, *3*, 10320.
[25] J. Kotakoski, A. V. Krasheninnikov, U. Kaiser, J. C. Meyer, *Phys. Rev. Lett.* **2011**, *106*, 105505.
[26] K. Chayambuka, G. Mulder, D. L. Danilov, P. H. L. Notten, *Adv. Energy Mater.* **2018**, *8*, 1800079.
[27] B. Zhang, C. M. Ghimbeu, C. Laberty, C. Vix-Guterl, J. M. Tarascon, *Adv. Energy Mater.* **2016**, *6*, 1501588.
[28] J. Yang, X. Zhou, D. Wu, X. Zhao, Z. Zhou, *Adv. Mater.* **2017**, *29*, 1604108.
[29] S. Alvin, C. Chandra, J. Kim, *Chem. Eng. J.* **2020**, *391*, 123576.
[30] D. Xu, C. Chen, J. Xie, B. Zhang, L. Miao, J. Cai, Y. Huang, L. Zhang, *Adv. Energy Mater.* **2016**, *6*, 1501929.
[31] L. Xiao, H. Lu, Y. Fang, M. L. Sushko, Y. Cao, X. Ai, H. Yang, J. Liu, *Adv. Energy Mater.* **2018**, *8*, 1703238.
[32] E. Olsson, T. Hussain, A. Karton, Q. Cai, *Carbon* **2020**, *163*, 276.
[33] E. Olsson, J. Cottom, H. Au, Z. Guo, A. C. S. Jensen, H. Alptekin, A. J. Drew, M.-M. Titirici, Q. Cai, *Adv. Funct. Mater.* **2020**, *30*, 1908209.
[34] E. Olsson, G. Chai, M. Dove, Q. Cai, *Nanoscale* **2019**, *11*, 5274.

[35] T. Hussain, E. Olsson, K. Alhameedi, Q. Cai, A. Karton, *J. Phys. Chem. C* **2020**, *124*, 9734.
[36] H. Alptekin, H. Au, A. C. S. Jensen, E. Olsson, M. Goktas, T. F. Headen, P. Adelhelm, Q. Cai, A. J. Drew, M.-M. Titirici, *ACS Appl. Energy Mater.* **2020**, *3*, 9918.
[37] K. Jurkiewicz, S. Duber, H. E. Fischer, A. Burian, *J. Appl. Crystallogr.* **2017**, *50*, 36.
[38] J. M. Stratford, P. K. Allan, O. Pecher, P. A. Chater, C. P. Grey, *Chem. Commun.* **2016**, *52*, 12430.
[39] C. Matei Ghimbeu, J. Górka, V. Simone, L. Simonin, S. Martinet, C. Vix-Guterl, *Nano Energy* **2018**, *44*, 327.
[40] S. Thinius, M. M. Islam, T. Bredow, *Surf. Sci.* **2016**, *649*, 60.
[41] S. Zhang, J. Northrup, *Phys. Rev. Lett.* **1991**, *67*, 2339.
[42] E. Olsson, J. Cottom, X. Aparicio-Anglès, N. H. de Leeuw, *Phys. Chem. Chem. Phys.* **2020**, *22*, 692.
[43] R. Grau-Crespo, S. Hamad, C. R. A. Catlow, N. H. de Leeuw, *J. Phys.: Condens. Matter* **2007**, *19*, 256201.
[44] B. Grabowski, T. Hickel, J. Neugebauer, *Phys. Status Solidi B* **2011**, *248*, 1295.
[45] C. Freysoldt, B. Grabowski, T. Hickel, J. Neugebauer, G. Kresse, A. Janotti, C. G. Van de Walle, *Rev. Mod. Phys.* **2014**, *86*, 253.
[46] F. Banhart, J. Kotakoski, A. V. Krasheninnikov, *ACS Nano* **2011**, *5*, 26.
[47] K. N. Kudin, B. Ozbas, H. C. Schniepp, R. K. Prud'homme, I. A. Aksay, R. Car, *Nano Lett.* **2008**, *8*, 36.
[48] K. Share, A. P. Cohn, R. Carter, B. Rogers, C. L. Pint, *ACS Nano* **2016**, *10*, 9738.
[49] B. Lee, M. Kim, S. Kim, J. Nanda, S. J. Kwon, H. D. Jang, D. Mitlin, S. W. Lee, *Adv. Energy Mater.* **2020**, *10*, 1903280.
[50] K. Wang, Y. Xu, Y. Li, V. Dravid, J. Wu, Y. Huang, *J. Mater. Chem. A* **2019**, *7*, 3327.
[51] R. Faccio, L. Fernández-Werner, H. Pardo, C. Goyenola, O. N. Ventura, A. W. Mombrú, *J. Phys. Chem. C* **2010**, *114*, 18961.
[52] O. V. Yazyev, L. Helm, *Phys. Rev. B: Condens. Matter Mater. Phys.* **2007**, *75*, 125408.
[53] Y. Zhang, S.-Y. Li, H. Huang, W.-T. Li, J.-B. Qiao, W.-X. Wang, L.-J. Yin, K.-K. Bai, W. Duan, L. He, *Phys. Rev. Lett.* **2016**, *117*, 166801.
[54] D. Datta, J. Li, V. B. Shenoy, *ACS Appl. Mater. Interfaces* **2014**, *6*, 1788.
[55] Y. Zhai, Y. Dou, D. Zhao, P. F. Fulvio, R. T. Mayes, S. Dai, *Adv. Mater.* **2011**, *23*, 4828.
[56] Z. Ju, P. Li, G. Ma, Z. Xing, Q. Zhuang, Y. Qian, *Energy Storage Mater.* **2018**, *11*, 38.
[57] T. Granzier-Nakajima, K. Fujisawa, V. Anil, M. Terrones, Y. T. Yeh, *Nanomaterials* **2019**, *9*, 425.
[58] P. Lazar, R. Mach, M. Otyepka, *J. Phys. Chem. C* **2019**, *123*, 10695.
[59] S. P. Kattel, B. Kiefer, P. Atanassov, *ECS Trans.* **2019**, *33*, 551.
[60] J. Yang, Z. Ju, Y. Jiang, Z. Xing, B. Xi, J. Feng, S. Xiong, *Adv. Mater.* **2018**, *30*, 1700104.
[61] C. Chen, Z. Wang, B. Zhang, L. Miao, J. Cai, L. Peng, Y. Huang, J. Jiang, Y. Huang, L. Zhang, J. Xie, *Energy Storage Mater.* **2017**, *8*, 161.
[62] J. S. Wei, T. B. Song, P. Zhang, X. Q. Niu, X. B. Chen, H. M. Xiong, *Mater. Chem. Front.* **2020**, *4*, 729.
[63] R. Zhang, H. Li, R. Li, D. Wei, W. Kang, Z. Ju, S. Xiong, *Chem. Commun.* **2019**, *55*, 14147.
[64] C. Yang, S. Xin, L. Mai, Y. You, *Adv. Energy Mater.* **2020**, *11*, 2000974.
[65] H. Zheng, Q. Qu, L. Zhang, G. Liu, V. S. Battaglia, *RSC Adv.* **2012**, *2*, 4904.
[66] S. Zhang, A. A. Teck, Z. Guo, Z. Xu, M.-M. Titirici, *Batteries Supercaps* **2020**, https://doi.org/10.1002/batt.202000306.
[67] J. Ye, H. Zhao, M. Kang, W. Song, Q. Kong, C. Chen, R. Wu, J. Mi, Z. Li, *Chem. Commun.* **2020**, *56*, 1089.
[68] Y. Li, M. Chen, B. Liu, Y. Zhang, X. Liang, X. Xia, *Adv. Energy Mater.* **2020**, *10*, 2000927.
[69] C. Matei Ghimbeu, B. Zhang, A. Martinez de Yuso, B. Réty, J. M. Tarascon, *Carbon* **2019**, *153*, 634.
[70] Y. Li, R. A. Adams, A. Arora, V. G. Pol, A. M. Levine, R. J. Lee, K. Akato, A. K. Naskar, M. P. Paranthaman, *J. Electrochem. Soc.* **2017**, *164*, A1234.
[71] Y. Huang, Y. Zheng, X. Li, F. Adams, W. Luo, Y. Huang, L. Hu, *ACS Energy Lett.* **2018**, *3*, 1604.
[72] V. L. Chevrier, G. Ceder, *J. Electrochem. Soc.* **2011**, *158*, A1011.
[73] J. M. Bray, C. L. Doswell, G. E. Pavlovskaya, L. Chen, B. Kishore, H. Au, H. Alptekin, E. Kendrick, M.-M. Titirici, T. Meersmann, M. M. Britton, *Nat. Commun.* **2020**, *11*, 2083.
[74] S. Alvin, D. Yoon, C. Chandra, H. S. Cahyadi, J. H. Park, W. Chang, K. Y. Chung, J. Kim, *Carbon* **2019**, *145*, 67.
[75] F. Xie, Z. Xu, Z. Guo, M.-M. Titirici, *Prog. Energy* **2020**, *2*, 042002.
[76] S. Alvin, H. S. Cahyadi, J. Hwang, W. Chang, S. K. Kwak, J. Kim, *Adv. Energy Mater.* **2020**, *10*, 2000283.
[77] D. A. Stevens, J. R. Dahn, *J. Electrochem. Soc.* **2001**, *148*, A803.
[78] H. Geng, Y. Peng, L. Qu, H. Zhang, M. Wu, *Adv. Energy Mater.* **2020**, *10*, 1903030.
[79] S. Huang, Z. Li, B. Wang, J. Zhang, Z. Peng, R. Qi, J. Wang, Y. Zhao, *Adv. Funct. Mater.* **2018**, *28*, 1706294.
[80] Y. Li, Y. Lu, P. Adelhelm, M.-M. Titirici, Y.-S. Hu, *Chem. Soc. Rev.* **2019**, *48*, 4655.
[81] Z. Jian, C. Bommier, L. Luo, Z. Li, W. Wang, C. Wang, P. A. Greaney, X. Ji, *Chem. Mater.* **2017**, *29*, 2314.
[82] P. C. Tsai, S. C. Chung, S. K. Lin, A. Yamada, *J. Mater. Chem. A* **2015**, *3*, 9763.
[83] J. Vandevondele, M. Krack, F. Mohamed, M. Parrinello, T. Chassaing, J. Hutter, *Comput. Phys. Commun.* **2005**, *167*, 103.
[84] J. VandeVondele, J. Hutter, *J. Chem. Phys.* **2007**, *127*, 114105.
[85] J. Hutter, M. Iannuzzi, F. Schiffmann, J. Vandevondele, *Wiley Interdiscip. Rev.: Comput. Mol. Sci.* **2014**, *4*, 15.
[86] K. Burke, F. G. Cruz, K.-C. Lam, *J. Chem. Phys.* **1998**, *109*, 8161.
[87] J. Perdew, K. Burke, M. Ernzerhof, *Phys. Rev. Lett.* **1996**, *77*, 3865.
[88] J. Perdew, K. Burke, M. Ernzerhof, *Phys. Rev. Lett.* **1997**, *77*, 1396.
[89] M. Guidon, J. Hutter, J. VandeVondele, *J. Chem. Theory Comput.* **2010**, *6*, 2348.
[90] A. D. Becke, E. R. Johnson, *J. Chem. Phys.* **2005**, *123*, 154101.
[91] E. R. Johnson, A. D. Becke, *J. Chem. Phys.* **2006**, *124*, 174104.
[92] S. Grimme, S. Ehrlich, L. Goerigk, *J. Comput. Chem.* **2011**, *32*, 1456.
[93] S. Grimme, J. Antony, T. Schwabe, C. Mück-Lichtenfeld, *Org. Biomol. Chem.* **2007**, *5*, 741.
[94] S. Grimme, J. Antony, S. Ehrlich, H. Krieg, *J. Chem. Phys.* **2010**, *132*, 154104.
[95] K. Momma, F. Izumi, *J. Appl. Crystallogr.* **2011**, *44*, 1272.